Plasmonic Split–Trench Resonator for Trapping and Sensing

Daehan Yoo,[†] Avijit Barik,[†] Fernando de León-Pérez,[‡,¶] Daniel A. Mohr,[†]

Matthew Pelton,[§] Luis Martín-Moreno,[¶] and Sang-Hyun Oh[*,†]

[†]*Department of Electrical and Computer Engineering, University of Minnesota,*
Minneapolis, Minnesota 55455, United States

[‡]*Centro Universitario de la Defensa de Zaragoza, E-50009 Zaragoza, Spain*

[¶]*Instituto de Nanociencia y Materiales de Aragón (INMA) and Departamento de Física de*
la Materia Condensada, CSIC-Universidad de Zaragoza, E-50009 Zaragoza, Spain

[§]*Department of Physics, University of Maryland, Baltimore County, Baltimore, Maryland*
21250, United States

E-mail: sang@umn.edu

Abstract

On-chip integration of plasmonics and electronics can benefit broad applications in biosensing, signal processing, and optoelectronics. A key requirement is a chip-scale manufacturing method. Here we demonstrate a split-trench resonator platform that combines a high-quality-factor resonant plasmonic biosensor with radiofrequency (RF) nanogap tweezers. The split-trench resonator can simultaneously serve as a dielectrophoretic trap and a nanoplasmonic sensor. Trapping is accomplished by applying a radio-frequency electrical bias across a 10-nm gap, thereby either attracting or repelling analytes. Trapped analytes are detected in a label-free manner using refractive-index sensing, enabled by interference between surface-plasmon standing waves in the trench and light transmitted through the gap. This active sample concentration mechanism enables detection of nanoparticles and proteins at a concentration as low as 10 pM. We can manufacture centimeter-long split-trench resonators with high throughput *via* photolithography and atomic layer deposition, toward practical applications in biosensing, spectroscopy, and optoelectronics.

Keywords

plasmonics, extraordinary optical transmission, dielectrophoresis, trapping, Fano resonance, atomic layer deposition

On-chip integration of sub-wavelength optics with electronics is a key theme in the field of plasmonics.[1–3] Metal slits with a nanometer-scale separation can be engineered to function as both plasmonic resonators and nanoelectrodes. Resonant interaction of light with surface-plasmon waves in a nanometer-scale slit can lead to highly concentrated optical fields within the slit.[4–13] While an isolated nanoslit by itself cannot couple light efficiently and create strong resonances in the visible or near-infrared regime, researchers have demonstrated ways to enhance light transmission by using periodic slit arrays,[14] a grating-coupled slit,[10] or a cavity-coupled slit.[15–18] Related structures utilizing a metal wedge[19] or a buried slit[18] have shown resonances with high quality factors, Q. While these reflector-coupled plasmonic resonators show promise, all of the aforementioned structures were made using focused-ion-beam (FIB) milling, a slow, serial process that does not enable fabrication of the large-scale chips that are needed for practical applications. Furthermore, sub-10-nm slits, which are desirable for tight confinement of electromagnetic fields,[20,21] cannot be easily milled with FIB.[22]

In addition to concentrating optical fields, narrow metallic slits can concentrate radio-frequency (RF) fields produced by electrically biasing the gap, producing strong field gradients analogous to the fringe field of a parallel-plate capacitor. These high-gradient fringe fields, in turn, can be used for dielectrophoretic trapping.[23,24] The phenomenon of dielectrophoresis (DEP) is an RF analog of the optical trapping process, *i.e.*, a movement of a polarizable particle in a spatially non-uniform electric field. The forces that move the particle originate from a net polarization induced by the difference in conductivity and dielectric permittivity between the particle and its surrounding medium.[25] The magnitude and direction of the DEP force acting on a particle are controllable with both the amplitude and frequency of AC voltage applied to the electrodes.[25]

Importantly, DEP is a scalable technique that can be naturally integrated with nanoplasmonics, since noble-metal plasmonic devices such as nano-apertures, slits, and sharp tips

can also act as electrodes for generating high-gradient fields for DEP. Indeed, DEP has been combined with plasmonic sensors in recent works, including nanohole DEP-enhanced sensing[26–28] and Raman spectroscopy.[29–31] Recent work used gold nanogap structures for DEP trapping of nanoparticles and combined fluorescence imaging,[23] but integrated real-time SPR sensing was not possible in such gaps, since an isolated slit generally does not possess distinct plasmonic resonances. In order to combine a nanoplasmonic sensing capability with the RF trapping capability of the nanoslit, it is necessary both to engingeer the plasmonic resonances of the structure and to develop a robust process for fabrication of nanogaps that can withstand relatively high bias voltages ($\sim$5V) without breakdown.

In this work, we demonstrate a practical approach to mass-produce centimeter-long plasmonic trench resonators fed by a sub-10-nm slit that can also be electrically biased. Our high-throughput fabrication scheme requires only photolithography and atomic layer deposition (ALD) to define trench resonators with sub-10-nm slits. We optimize the interaction of plasmon resonances in the trench with direct optical transmission through the nanogap to obtain a high-Q transmission peak, which is used for real-time biosensing. The slit within the trench resonator also enables DEP-enhanced trapping of analytes, allowing for dynamic plasmonic biosensing of nanoparticles and protein molecules at concentrations as low as 10 pM.

Results and discussion

Split-trench resonator. In our device structure, shown in Figure 1(a), light traversing upwards through the slit is diffracted into two different radiation channels: free-space modes are radiated to the far field, while evanescent surface-plasmon (SPP) modes launched by the nanoslit propagate along the metal surface. These SPP modes travel toward the sidewalls of the trench resonator, reflect back, and interfere with light directly transmitted through the nanoslit. The result is a standing-wave pattern that can be analytically described using a

simple interferometric approximation.[17,32–34] A traveling SPP wave experiences a total round trip phase delay,

$$\theta = 2 \times \frac{2\pi}{\lambda_{SPP}} L + \phi_r, \tag{1}$$

with respect to the light transmitted directly through the nanogap, where ϕ_r is the phase shift from plasmon reflection, $\lambda_{SPP} = \lambda_0 \sqrt{(\epsilon_d + \epsilon_m)/(\epsilon_d \epsilon_m)}$ is the wavelength of the SPP, and L is the distance between the slit and the sidewall. Interference occurs when the total phase delay is a multiple of π, such that $\theta = n\pi$, where the integer n is the diffraction order.

The total power radiated to the far field is obtained from the integration of the vertical component of the time-averaged Poynting vector, $S_y = -\mathrm{Re}[E_x H_z^*]/2$. For a given mode, the z-component of the magnetic field is proportional to the x-component of the electric field, i.e., $H_z = Y_k E_x$, where Y_k is the modal admittance. Modeling the light transmitted through our structures thus requires consideration only of E_x for a particular mode. Assuming perfect electric conductor (PEC) sidewalls, which is a good approximation when L is much larger than the metal skin depth, gives $E_y = 0$ at the sidewalls; Maxwell's equation $\nabla \cdot \mathbf{E} = 0$ then requires that E_x have a maximum at the sidewalls, corresponding to $\phi_r = 0$. The resulting standing waves are cosine functions with an integer number of half-wavelengths along the length $2L$. From Eq. 1, we thus have for E_x

$$2L = \frac{\lambda_{SPP}}{2} n, \ \text{with } n = 1, 2, 3, \ldots, \tag{2}$$
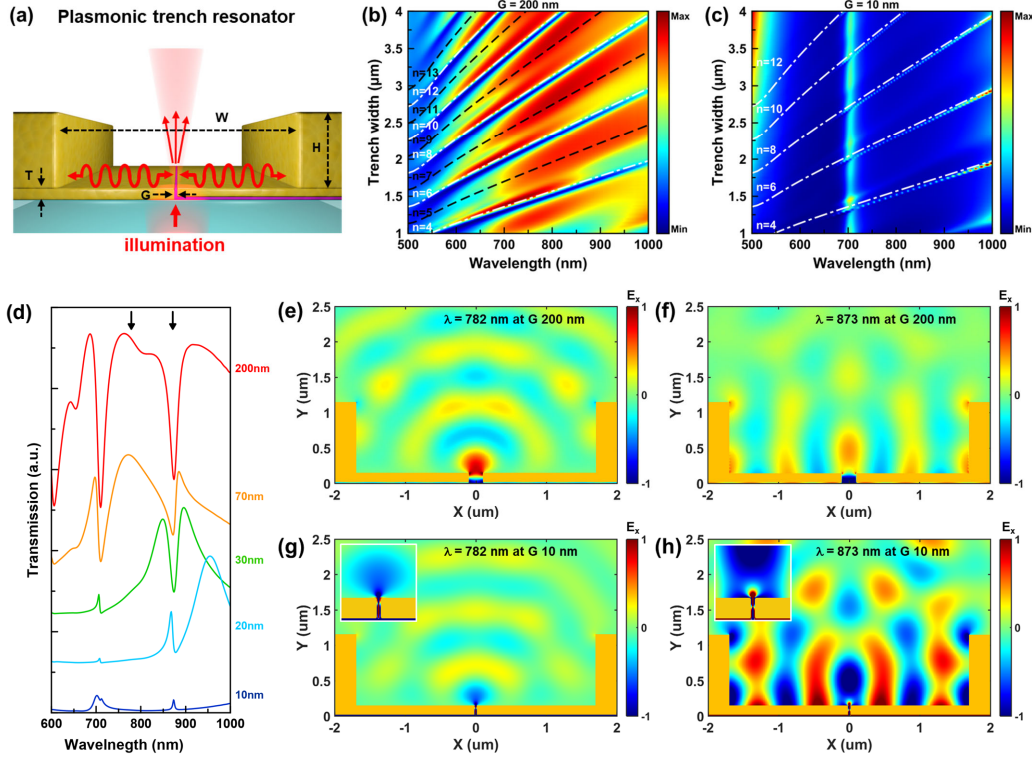
Figure 1: **Split-trench resonator architecture and optical response.** (a) The resonator consisting of a metal film, a feed gap, and sidewall mirrors. In the trench, surface plasmon waves excited by illuminating the sub-wavelength slit feed cavity resonances and create plasmonic standing waves. Calculated optical transmission spectra show complex resonances formed by the interference between surface-plasmon modes inside the trench and light transmitted directly through the slit. (b-c) Dispersion maps for trench resonators with (b) 200-nm gaps and (c) 10-nm gaps drilled in 130-nm thick gold films. White dashed lines indicate the constructive condition of the in-plane component of the eletric field, E_x, for even diffraction orders, n (see Eq. 2), and black dashed lines represent the destructive condition for odd orders. (d) Transmission spectra, simulated using the finite-difference time-domain (FDTD) method, for trench resonators of width $W = 3.4$ μm with increasing gap sizes. (e,f) E_x at diffraction orders (d) $n = 9$ and (e) $n = 8$ in the trench resonator with a 2000-nm gap. (g,h) E_x at the same diffraction orders but with a 10-nm gap.

When the feed gap is centered at the cavity of width $W \equiv 2L$, constructive (destructive) interference at the gap position occurs for even (odd) values of n in Eq. (2). Figure 1 compares the dispersion characteristics simulated for a trench resonator fed by (b) 200-nm and (c) 10-nm gaps with the interference condition of Eq. (2). Constructive interference given

by even values of n in Eq. (2) fit well with transmission dips simulated by finite-difference time-domain (FDTD) modeling (white dash-dotted line), while destructive interference given by odd values of n fit well with transmission peaks (black dashed line).

However, secondary peaks are found between the two interference conditions. Moreover, this simple interferometric analysis seems no longer valid for the trench resonator with a 10-nm slit in Figure 1(c), for which transmission peaks as well as dips occur along with the constructive interference condition. To understand the cause of this deviation, we investigated the transmission spectra while sequentially reducing the gap size from 200 nm to 10 nm for a fixed trench width of W=3.4 μm in a spectral window where diffraction orders n=8, 9, and 10 can be excited. As shown in Figure 1(d), the dip position does not shift, but rather transforms from a dip into an asymmetric peak with decreasing gap size.[35–39]

Such spectral features may be understood by taking into account the coupling of vertical Fabry-Perot (FP) modes inside the slit[4] and lateral SPP cavity modes in the trench.[15] The FP modes present here are similar to those found in single slits by themselves: they are characterized by broad transmission peaks, whose spectral linewidth decreases when the gap size is reduced, as illustrated in Figure 1(d). When the vertical FP modes couple to lateral SPP cavity resonances in the trenches, hybrid modes are formed, with narrow resonances having characteristic asymmetric Fano lineshapes.[38,40,41]

The E_x-field profiles provide further information about the coupling of FP and SPP resonances. The coupling of each mode in the slit with each of the standing waves in the trench can be quantified by the overlap integral of their respective E_x components. For the sub-wavelength apertures considered in this work, we can assume that only the fundamental transverse mode with constant amplitude along the aperture width is excited inside the slit. A qualitative understanding of the FP-SPP coupling can thus be obtained by examination of the electric-field map for this mode and the field map for the SPP mode with the same resonance wavelength.

Figure 1(e)-(h) show FDTD-simulated E_x fields at both destructive ($n = 9$ at $\lambda = 782$ nm) and constructive ($n = 8$ at $\lambda = 873$ nm) interference conditions for gap widths $G = 10$ nm and $G = 200$ nm. When $n = 9$ half wavelengths are accommodated in the trench, E_x becomes asymmetric with respect to the slit center, resulting in small overlap between the SPP and FP modes (the overlap is equal to zero for ideal PEC walls in both trench and gap). The small coupling prevents the excitation of odd diffraction orders by the fundamental mode of the gap. In fact, the E_x field profiles at $\lambda = 782$ nm depicted in Figures 1(e) and (g) for the 200 nn and 10 nm gap, respectively, resemble the radiation pattern of a single slit without a cavity, which is characterized by concentric semicircular wave fronts radiated from the aperture. The radiation patterns are quite similar for both gap sizes despite the different fields excited inside the two gaps. However, the resulting transmittance, reported in Figure1(d), is much larger for the wider gap.

On the other hand, for even diffraction orders, the FP resonance of the slit couples with cavity modes to form standing waves, evident as vertical fringes in Figures 1(f) and (h). When the slit is 200 nm wide, the amplitude of the fringes is similar to the single slit case, as the interaction with the cavity mode mainly produces additional fringes in the existing single slit field profile. In this case, a new scattering channel is opened along the metal surface which drastically reduces the intensity of the radiated light at the given wavelength, as shown in Figure1(d), and the lost optical power is mainly absorbed by the metal. By contrast, when the slit size is reduced down to 10 nm, weaker coupling with the cavity modes produces a stronger stationary field profile with larger amplitude, inducing a sharp Fano transmission peak, as shown in Figure1(d). A rigorous mathematical description of the electromagnetic (EM) fields excited in the cavity can be found the SI.
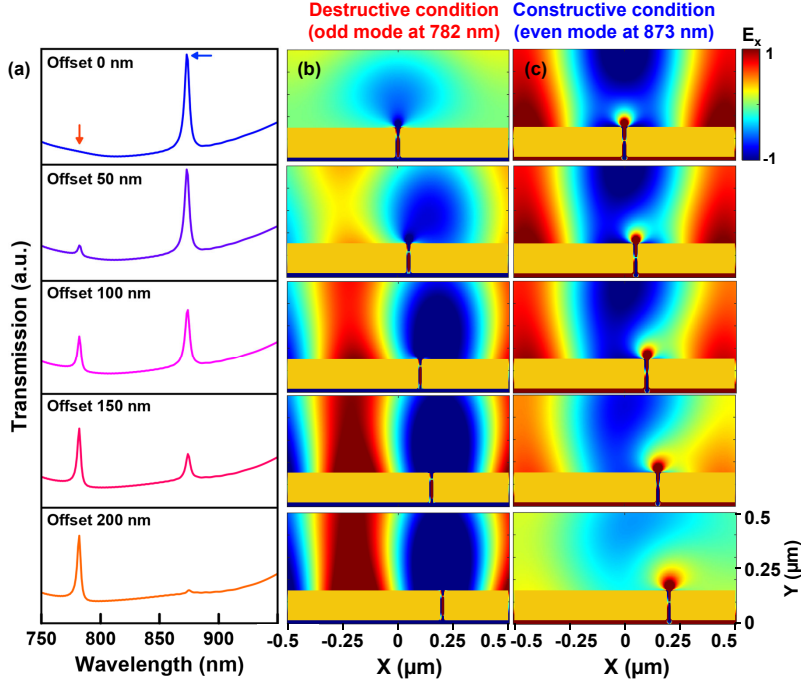
8

Figure 2: **Tuning the Fano resonances.** (a) Transmission spectra, simulated using the finite-difference time-domain method, for trench resonators with slits at different positions, from 0 nm to 200 nm, relative to the center. (b,c) Spatial distributions of the E_x field component in the corresponding trench resonators for wavelengths of (b) 782 nm ($n = 9$) and (c) 873 nm ($n = 8$). Column (b) shows the appearance of a forbidden mode at the destructive-interference condition when the geometrical symmetry is broken. Column (c) shows the extinction of a resonance peak at the constructive-interference condition as the nanogap moves to the right.

Tuning the Fano resonances. Computer simulations, shown in Figure 2, illustrate how the Fano resonances evolve as a function of the slit position relative to the center of the trench resonator. When the slit is in the center of the trench, a transmission peak for the 10-nm gap is observed at 873 nm where the constructive condition for $n = 8$ is met, whereas there is no transmission peak at the destructive condition ($n = 9$, $\lambda = 782$ nm). However, as the nanogap position shifts to the right, the suppressed mode at the destructive condition starts to be excited, while the Fano resonance at the constructive condition simultaneously begins to decrease. This can be understood as being due to increased overlap of the FP

mode with the even mode as the slit moves off center and decreased overlap with the odd mode, as illustrated by the corresponding field maps in Figure 2(b-c).

We note that both peaks can be excited simultaneously and that the linewidth of the Fano resonances can be made much narrower than conventional surface-plasmon resonances by engineering the intereeence effect and the structural symmetry[36,38] The narrower linewidth provides higher a higher figure of merit in refractive-index sensing applications.[37,39,42] Together with the ability of the slits to concentrate analytes through DEP, the Fano resonances thus enable the split-trench resonators to serve as sensitive molecular sensors.

Scalable fabrication *via* atomic layer lithography. The main objective in designing our trench resonator is to shrink the gap size towards 10 nm to create strong DEP trapping forces at low bias voltages while maintaining a narrow resonance peak that can be measured with a high signal-to-noise ratio. To obtain sufficiently high photon counts for real-time SPR sensing with transmitted light through such a narrow gap, the gap and integrated reflectors should be made very long in the orthogonal direction. It is not trivial to directly pattern a 10-nm gap at the wafer scale using conventional FIB or electron-beam lithography. In contrast, our ALD-based approach (in Figure 3) decouples the gap patterning resolution from the gap length and density. We can thus readily produce a 10-nm gap with 1-μm-tall sidewall mirrors extending over 1 cm.

The fabrication process is illustrated in Figure 3 (a-b). First, photolithography (using MA-6 mask aligner), metal deposition, and lift-off are used to create an array of Au rectangles (130 nm thickness and 1 cm by 0.1 cm side lengths). After coating a 10-nm-thick Al_2O_3 ALD layer on the top surface and sidewalls of the Au rectangles, another Au layer (120 nm thickness) is directionally evaporated (Figure 3a). The portion of the second Au layer sitting atop the first Au pattern is then peeled off using adhesive tape (3M Scotch Magic tape), creating an array of centimeter-long and 10-nm-wide nanogap structures filled with Al_2O_3. Next, the long nanogap is divided into multiple devices using photolithography and blanket

(a) Fabrication of a centimeter-long nanogap using atomic layer lithography

1st Au

Al₂O₃

2nd Au

Nanogap

(b) Electrode patterning and formation of trench sidewalls

PR

(c)

(d)

(e)

2mm

Al₂O₃ 10 nm

1 μm

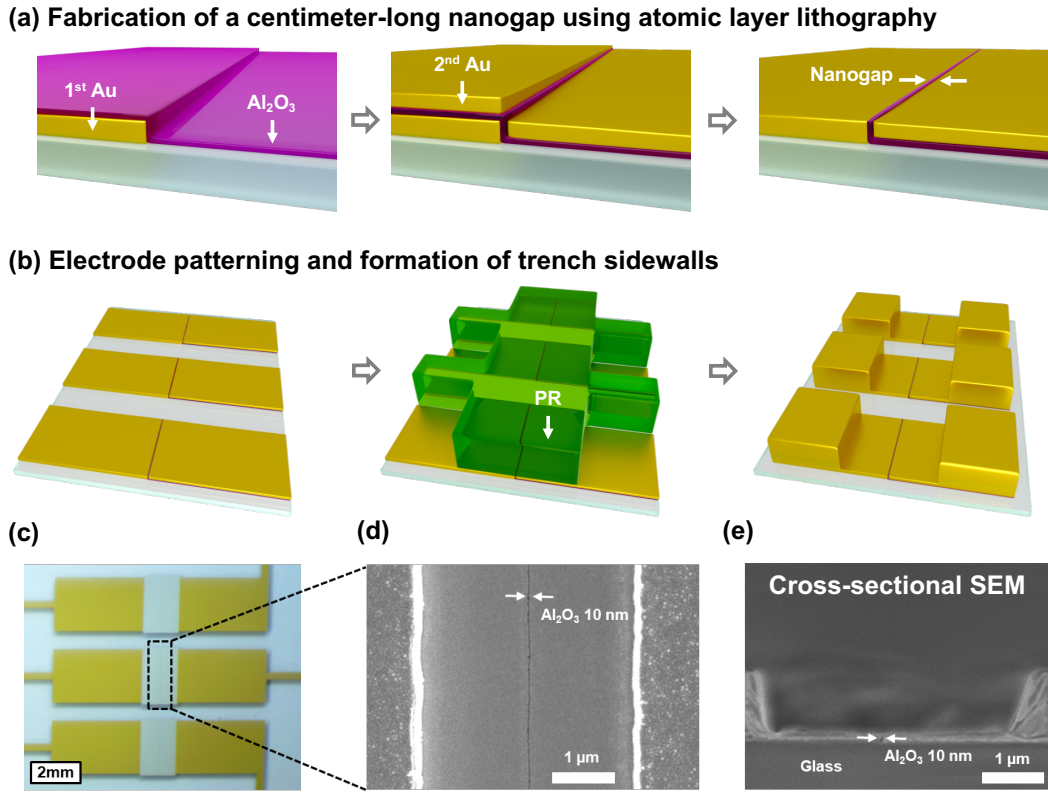Cross-sectional SEM

Glass

Al₂O₃ 10 nm

1 μm

Figure 3: **Device fabrication *via* atomic layer lithography.** (a) High-throughput batch fabrication of centimeter-long arrays of trench resonators using atomic layer deposition and photolithography. (b) Patterning a single nanogap structure and integration of sidewalls. (c) Optical-microscope image of a chip including multiple trench resonators. (d) Top-down scanning electron micrograph (SEM) of trench resonator. (e) Cross-sectional SEM of trench resonator.

ion milling (Figure 3b), followed by another photolithography step that will eventually define the sidewall mirrors. Ion milling is then performed to eliminate the Al₂O₃ coated on the first Au layer, and then a 1-μm-thick Ag evaporation and liftoff process is performed, completing the device: electrodes split by a 10-nm feed gap in a Au film and 1-μm-tall Ag cavity walls. Figure 3c shows an image of the chip with multiple trench nanogap resonators. As shown in scanning electron micrograph (SEM) images (Figures 3d and e), a 10-nm Al₂O₃-filled nanogap is situated in the trench whose width and height are 3.4 μm and 1 μm, respectively.

11

Optical characterization. We measured the optical transmission spectra of the trench resonators immersed in water. Based on the analysis shown in Fig. 2, we made devices with various offset distances between the slit and the center of the trench resonator. We measured the optical transmission spectra of these devices immersed in water, and we empirically chose the optimal device that gave the highest transmission intensity and narrowest transmission spectrum (Fig. 4(a)). The offset distance for this device was measured by SEM to be 1,450 nm, as shown in Figure 4b.

FDTD simulations were performed to identify the physical origin of the multiple resonance peaks in the measured transmission spectrum. The contours of the fabricated device, such as angled sidewalls and rounded top corners, were reflected in the modeling to improve agreement with experimental results. As shown in Figure 4a, the FDTD results can accurately model the frequency of each resonance peak, although the transmission intensity and linewidth do not agree well. As shown in Figure 4d, the electric field at 770 nm (830 nm) shows thirteen (twelve) fringes existing across the water-filled trench; the resonance peak at 770 nm thus arises from constructive interference (odd mode), and the resonance peak at 823 nm arises from destructive interference (even mode).

We used this device for bulk refractive-index (RI) sensing (Figure 4c), obatining a sensitivity of 687 nm/RIU for both modes, comparable to previous results obtained from other nanoplasmonic devices.[43] Similar measurements with thin films gave a shift of 21 nm for a 20-nm-thick SiO_2 ALD coating. Although this refractive-index sensitivity lags behind conventional prism-based surface-plasmon refractometers in terms of bulk RI sensitivity,[44] the split-trench resonator offers a simpler optical illumination scheme combined with quicker detection capabilities. Moreover, it can inherently be integrated with DEP concentration and trapping of nanoparticles and biomolecules, enabling detection of analytes at low concentration in solution.

RF dielectrophoresis with electrically biased split-trench resonators. The advan-
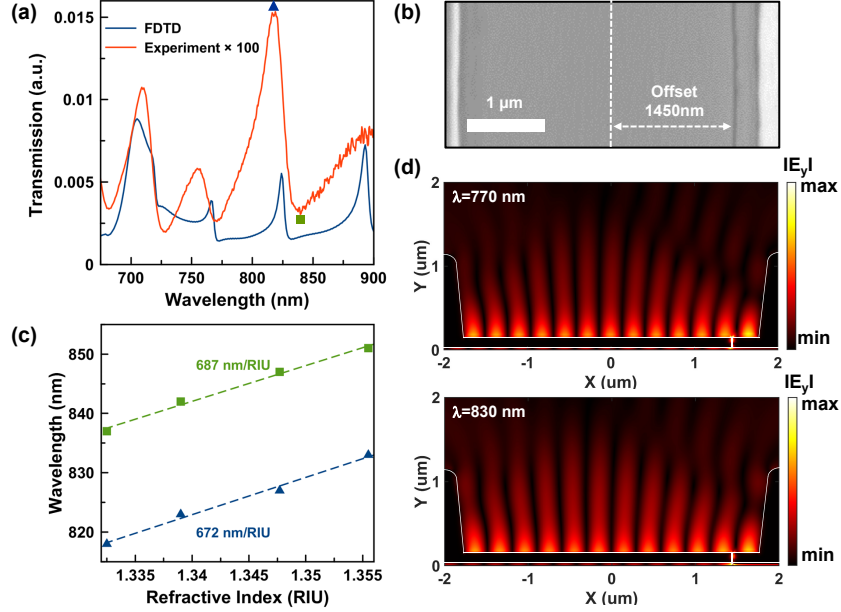
Figure 4: **Optical characterization.** (a) Optical transmission spectrum from an asymmetric trench-resonator biosensor immersed in water. A computer-simulated spectrum (blue solid line) is compared with the experimentally measured one (red). (b) SEM image of the asymmetric trench nanogap resonator. The offset of the slit from the center of the trench resonator is 1,450 nm. (c) Measurements of bulk refractive index sensitivity. (d) Simulated electric field distributions for the asymmetric trench resonator in water at the wavelengths of 770 nm (top) and 830 nm (bottom).

tages of the trench resonators, particularly their ability to simultaneously perform DEP trapping, enable them to act as real-time plasmonic biosensors. Figure 5(a) conceptually illustrates the operation of this device.

We find that the 10-nm-thick Al_2O_3 layer in the slit can withstand an applied voltage of up to 5 V without breakdown. A voltage as low as 1 V across this gap creates an extremely high electric field $|E|$ of 10^7 V/m, thus boosting the electric field gradient and the DEP force given by

13

$$\mathbf{F}_{DEP}(\omega) = \pi\epsilon_m R^3 \Re[f_{CM}(\omega)]\nabla|\mathbf{E}|^2, \tag{3}$$

where R is the radius of a spherical particle, ϵ_m is the permittivity of the surrounding medium, $|E|$ is the magnitude of the electric field, and $\Re[f_{CM}(\omega)]$ is the real component of the frequency-dependent Clausius-Mossotti (CM) factor, given by

$$f_{CM}(\omega) = \frac{\epsilon_p^*(\omega) - \epsilon_m^*(\omega)}{\epsilon_p^*(\omega) + 2\epsilon_m^*(\omega)}, \tag{4}$$

where ϵ_p and ϵ_m are the complex permittivities of the particle and the surrounding medium, respectively. A positive CM factor results in a DEP force that attracts particles to the nanogap, a negative $f_{CM}(\omega)$ results in the repulsion of particles, as illustrated in Figure 5a.

For initial DEP trapping experiments, fluorescent polystyrene (PS) beads (190 nm diameter, 600 nm emission wavelength, Bangs Laboratories, Fishers, IN) were diluted 100-fold in DI water. The motion of the PS beads was recorded at regular time intervals of 1 s using a microscope with a Photometrics CoolSNAP HQ2 CCD camera and Mirco-Manager software. The video clip of the DEP trapping process is included in the SI; snapshots are shown in Figure 5(b).

Next, a DEP-enhanced real-time plasmonic sensing experiment was performed using these 190-nm PS beads (Figure 5c). After 50 s of idle time at zero bias, a 1-MHz RF bias was applied across the slit, and the voltage peak-to-peak amplitude was increased by 0.1 V every 50 s. Trapping was first observed as a shift in the optical transmission spectrum through the slit for a bias of 0.4 V, and trapping of additional beads was observed as successively larger shifts as the voltage increased further. Next, the frequency was switched to 10 MHz, which resulted in an abrupt drop in the spectral shift due to a negative DEP force (repulsion). One cycle of positive and negative DEP was repeated before the voltage bias was removed at 700 s, and a steady baseline was maintained for 50 s.
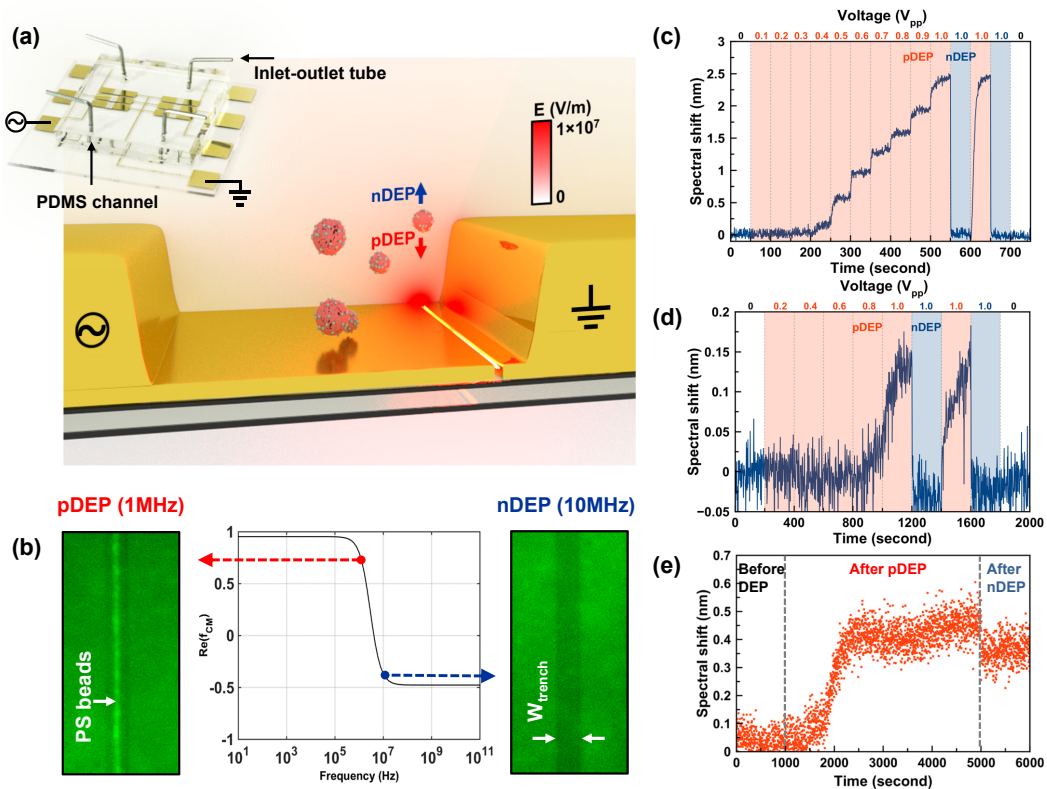
Figure 5: **DEP-enhanced plasmonic sensing.** (a) Conceptual illustration of DEP forces attracting biomolecules towards an RF-biased slit (pDEP) or repelling them away (nDEP). Overlaid is the simulated electric field of a 1 V bias applied across a 10-nm gap. The inset contains a photograph of a six-device chip with PDMS microfluidics. (b) The real part of the Clausius-Mossotti factor, $\Re[f_{CM}(\omega)]$, for suspended polystyrene (PS) beads (measured conductivity: 0.28 mS/m) as a function of RF frequency. Side panels contain fluorescence images of 190-nm PS beads attracted to (1 MHz) and repelled from (10 MHz) the nanogap. (c) Optical transmission resonance shift as a function of applied voltage, (V_{pp} from 0 to 1 V), and time as 190-nm PS beads are trapped. (d) Same as (c), except with 30-nm PS beads. (e) Spectral shift as bovine serum albumin molecules (10 pM concentration) are trapped with a positive DEP bias of 5 V and 1 kHz frequency. After 5000 s, a 10 MHz frequency is applied, and the DEP becomes negative.

Next, we experimented with 30 nm PS beads, where we observed the onset of trapping at 0.8 V (Figure 5d). By alternating the RF drive frequency between 1 MHz and 10 MHz, we can switch between positive and negative DEP regimes, respectively, and observe sudden signal drops.

Finally, bovine serum albumin (BSA, Sigma-Aldrich) was used to demonstrate DEP-enhanced plasmonic biosensing of low-concentration protein molecules (Figure 5e). BSA was dissolved in water at a concentration of 10 pM. The solution was then injected into the microfluidic channel using a syringe pump at a flow rate of 50 μl/hr. Optical transmission spectra through the trench resonator were recorded every 2 s. After 1,000 s idle time, an RF bias of 5 V and a frequency of 1 kHz was switched on. The onset of trapping was observed at 1,500 s, and the spectral shift gradually saturated. At 5,000 s, the RF frequency was switched to 10 MHz, corresponding to negative DEP, and the signal dropped. The spectral shift did not return to the original baseline level after the negative DEP step, which is likely due to nonspecific binding of BSA molecules on the surface. Using this data, we conclude the trench resonator is capable of detecting 10 pM BSA molecules within 1,500 s *via* nanogap DEP. With DEP concentration, the measured detection time, defined as the time it takes to concentrate analytes and generate a signal 3× higher than the noise floor, was 20 min, which is 23× faster than the diffusion-limited detection time.

Conclusions

We have presented theory, computational simulations, a scalable fabrication technique, sub-volt DEP trapping, and refractive-index-based biosensing for trench resonators with sub-10 nm gaps. The combination of the narrow Fano resonance and the strong AC electric field created across the 10-nm gap electrode enables rapid trapping of nanoparticles and biomolecules and concurrent label-free detection. Furthermore, the DEP-enhanced plasmonic biosensor can overcome diffusion-limited transport, significantly reducing the time of detection and enabling the detection of analyte at a concentration as low as 10 pM.

A wide range of plasmon-enhanced diagnostic sensors[45–49] can benefit from this DEP-enhanced analyte transport scheme. Our electrically biased split-trench resonator can also benefit applications in nanophotonics, optoelectronics, and signal processing applications.[50] Since a

large number of quantum emitters (*e.g.*, quantum dots and nanodiamonds) can be trapped at the centimeter-long nanogap, one can study strong light-matter interactions[51] and electrical carrier injection and electroluminescence[52–56] using this platform.

Methods

Device fabrication. Three mask layers were used to fabricate the resonant trench nanogap electrodes. For the first lithography step, negative photoresist (NR71-1500P) was spin-coated on a glass wafer at 5,000 rpm for 60 s. After a soft bake step at 150 °C for 60 s, rectangular patterns (10 mm × 0.1 mm) were transferred onto the photoresist-coated wafer *via* an MA-6 contact aligner with a dark-field Cr mask, followed by a post-exposure bake at 100 °C for 60 s and a developing process using RD 6. The metal deposition (130 nm Au with 5 nm Ti adhesion layer) *via* an electron-beam evaporator (Temescal) and lift-off in a solvent (1165 remover) created the first Au rectangular hole patterns. The patterned metal film was then conformally coated with a 10-nm-thick Al_2O_3 layer using ALD at 250 °C with a deposition rate of 1.1 Å/cycle (Cambridge NanoTech Inc., Savannah). Next, directional evaporation (Temescal) was used to deposit a second Au film with a thickness of 120 nm, filling the rectangular hole patterns in the first Au film. The portion of the second Au film deposited atop the patterned first Au film was then removed using single-sided 3M Scotch Magic tape, which created vertically oriented Al_2O_3 gaps in the two Au films along the perimeter of the rectangular patterns. In the second lithography step, the positive photoresist (S1813) was employed with a bright field Cr mask. The nanogap patterns were spin-coated with photoresist at 5,000 rpm for 60 s. After a soft bake at 115 °C for 60, the second layer patterns were transferred to the resist *via* an MA-6 contact aligner and developed using a mixture of 351 Developer:H_2O (1:5). An ion milling step (Intlvac) was then used to pattern the 1-cm-long nanogap into three seperate 2-mm-long nanogap electrodes. In the final photolithography step, positive photoresist (S1818) was used to build the trench structure. The fabricated nanogap electrodes were spin-coated with resist at 2,000 rpm for 60 s and baked at 115 °C for another 60 s. The third layer patterns were created on top of the nanogap electrodes after the exposure and developing processes, followed by evaporation of 1-μm-thick Ag using electron-beam evaporation (Temescal) and lift-off in solvent (1165 remover) to create a trench along the gap.

Optical measurement of the split-trench resonator. Visible wavelength transmission measurements of the trench resonator were performed by illuminating the structures with a halogen lamp source through a condenser on an inverted microscope (Nikon, Ti-S), and the transmitted light was collected using a $10\times$ objective and imaged onto the 200-μm-wide entrance slit of a 300 mm focal length imaging spectrometer (Acton SP2300i) equipped with a CCD camera (Princeton, Pixis 400). Spectra were background-subtracted and normalized using the spectrum for direct transmission through the glass substrate.

FDTD optical modeling. Lumerical FDTD software was employed for computational modeling. Perfectly matched layer absorbing boundary conditions were chosen in the x and y directions to absorb transmitted and reflected light from the structure. A plane wave illuminated the split-trench structure from below at normal incidence. A mesh size of 1 nm was used for resolving the 10 nm gap structure.

Microfluidic flow cell. For real-time kinetic measurements and DEP trapping experiments, we fabricated microfluidic channels *via* polydimethylsiloxane (PDMS, Sylgard 184) soft lithography. We grew a 20-nm SiO_2 layer on the metallic surface of trench resonator by ALD. The surfaces of the SiO_2-coated trench resonator and the PDMS channels were treated in O_2 plasma for 30 s and were bonded to form a flow cell. The chip was then placed on a hot plate at 70 °C for 5 min to promote covalent PDMS-SiO_2 bonding.

Associated content

Supporting information

Semi-analytical description of the transmission spectra *via* a coupled-mode method (CMM). Supplementary video file shows the process of dielectrophoretic manipulation of 190-nm-sized polystyrene beads using the split-trench resonator device (5x real time).

This material is available free of charge *via* the Internet at http://pubs.acs.org

Author information

Author contributions

D.Y., D.A.M. and S.-H.O. were responsible for the development of the trench resonator structure. D.Y. and A.B. performed particle trapping experiments. L.M.-M, F.d.L.-P., and M.P. were responsible for the theoretical analysis. All authors contributed to writing the paper.

Competing interests

The authors declare no competing financial interest.

Acknowledgement

References

1. Atwater, H. A. The Promise of Plasmonics. *Scientific American* **2007**, *296*, 56–63.

2. Ebbesen, T. W.; Genet, C.; Bozhevolnyi, S. I. Surface-Plasmon Circuitry. *Physics Today* **2008**, *61*, 44.

3. Brongersma, M. L.; Shalaev, V. M. The Case for Plasmonics. *Science* **2010**, *328*, 440–441.

4. Miyazaki, H. T.; Kurokawa, Y. Squeezing Visible Light Waves into a 3-nm-Thick and 55-nm-Long Plasmon Cavity. *Physical Review Letters* **2006**, *96*, 097401.

5. Dionne, J.; Sweatlock, L.; Atwater, H.; Polman, A. Plasmon Slot Waveguides: Towards Chip-Scale Propagation with Subwavelength-Scale Localization. *Physical Review B* **2006**, *73*, 035407.

6. Maier, S. A. *Plasmonics: Fundamentals and Applications*, 1st ed.; Springer: New York, NY, 2007.

7. Baumberg, J. J.; Aizpurua, J.; Mikkelsen, M. H.; Smith, D. R. Extreme Nanophotonics from Ultrathin Metallic Gaps. *Nature Materials* **2019**, *18*, 668–678.

8. Ebbesen, T. W.; Lezec, H. J.; Ghaemi, H.; Thio, T.; Wolff, P. Extraordinary Optical Transmission Through Sub-Wavelength Hole Arrays. *Nature* **1998**, *391*, 667–669.

9. Porto, J.; Garcia-Vidal, F.; Pendry, J. Transmission Resonances on Metallic Gratings with Very Narrow Slits. *Physical Review Letters* **1999**, *83*, 2845.

10. García-Vidal, F.; Lezec, H.; Ebbesen, T.; Martín-Moreno, L. Multiple Paths to Enhance Optical Transmission through a Single Subwavelength Slit. *Physical Review Letters* **2003**, *90*, 213901.

11. Martín-Moreno, L.; García-Vidal, F. J.; Lezec, H. J.; Degiron, A.; Ebbesen, T. W. Theory of Highly Directional Emission from a Single Subwavelength Aperture Surrounded by Surface Corrugations. *Physical Review Letters* **2003**, *90*, 167401.

12. García-Vidal, F. J.; Martín-Moreno, L.; Ebbesen, T. W.; Kuipers, L. Light Passing through Subwavelength Apertures. *Reviews of Modern Physics* **2010**, *82*, 729–787.

13. Rodrigo, S. G.; de León-Pérez, F.; Martín-Moreno, L. Extraordinary Optical Transmission: Fundamentals and Applications. *Proceedings of the IEEE* **2016**, *104*, 2288–2306.

14. García-Vidal, F.; Martín-Moreno, L. Transmission and Focusing of Light in One-Dimensional Periodically Nanostructured Metals. *Physical Review B* **2002**, *66*, 155412.

15. Min, Q.; Gordon, R. Surface Plasmon Microcavity for Resonant Transmission through a Slit in a Gold Film. *Optics Express* **2008**, *16*, 9708–9713.

16. Chen, J.; Li, Z.; Yue, S.; Xiao, J.; Gong, Q. Plasmon-Induced Transparency in Asymmetric T-Shape Single Slit. *Nano Letters* **2012**, *12*, 2494–2498.

17. Olson, S. A.; Mohr, D. A.; Shaver, J.; Johnson, T. W.; Oh, S.-H. Plasmonic Cup Resonators for Single-Nanohole-Based Sensing and Spectroscopy. *ACS Photonics* **2016**, *3*, 1202–1207.

18. Zhu, W.; Xu, T.; Wang, H.; Zhang, C.; Deotare, P. B.; Agrawal, A.; Lezec, H. J. Surface Plasmon Polariton Laser Based on a Metallic Trench Fabry-Perot Resonator. *Science Advances* **2017**, *3*, e1700909.

19. Kress, S. J.; Antolinez, F. V.; Richner, P.; Jayanti, S. V.; Kim, D. K.; Prins, F.; Riedinger, A.; Fischer, M. P.; Meyer, S.; McPeak, K. M.; Poulikakos, D.; Norris, D. J. Wedge Waveguides and Resonators for Quantum Plasmonics. *Nano Letters* **2015**, *15*, 6267–6275.

20. Ward, D. R.; Grady, N. K.; Levin, C. S.; Halas, N. J.; Wu, Y.; Nordlander, P.; Natelson, D. Electromigrated Nanoscale Gaps for Surface-Enhanced Raman Spectroscopy. *Nano Letters* **2007**, *7*, 1396–1400.

21. Im, H.; Bantz, K. C.; Lindquist, N. C.; Haynes, C. L.; Oh, S.-H. Vertically Oriented Sub-10-nm Plasmonic Nanogap Arrays. *Nano Letters* **2010**, *10*, 2231–2236.

22. Lindquist, N. C.; Nagpal, P.; McPeak, K. M.; Norris, D. J.; Oh, S.-H. Engineering Metallic Nanostructures for Plasmonics and Nanophotonics. *Reports on Progress in Physics* **2012**, *75*, 036501.

23. Barik, A.; Chen, X.; Oh, S.-H. Ultralow-Power Electronic Trapping of Nanoparticles with Sub-10 nm Gold Nanogap Electrodes. *Nano Letters* **2016**, *16*, 6317–6324.

24. Ertsgaard, C. T.; Wittenberg, N. J.; Klemme, D. J.; Barik, A.; Shih, W.-C.; Oh, S.-H. Integrated Nanogap Platform for Sub-Volt Dielectrophoretic Trapping and Real-Time Raman Imaging of Biological Nanoparticles. *Nano Letters* **2018**, *18*, 5946–5953.

25. Pethig, R. *Dielectrophoresis: Theory, Methodology and Biological Applications*, 1st ed.; John Wiley & Sons, Inc.: Hoboken, NJ, 2017.

26. Barik, A.; Otto, L. M.; Yoo, D.; Jose, J.; Johnson, T. W.; Oh, S.-H. Dielectrophoresis-Enhanced Plasmonic Sensing with Gold Nanohole Arrays. *Nano Letters* **2014**, *14*, 2006–2012.

27. Freedman, K. J.; Otto, L. M.; Ivanov, A. P.; Barik, A.; Oh, S.-H.; Edel, J. B. Nanopore Sensing at Ultra-Low Concentrations Using Single-Molecule Dielectrophoretic Trapping. *Nature Communications* **2016**, *7*, 10217.

28. Nadappuram, B. P.; Cadinu, P.; Barik, A.; Ainscough, A. J.; Devine, M. J.; Kang, M.; Gonzalez-Garcia, J.; Kittler, J. T.; Willison, K. R.; Vilar, R.; Actis, P.; Wojciak-

Stothard, B.; Oh, S.-H.; Ivanov, A. P.; Edel, J. B. Nanoscale Tweezers for Single-Cell Biopsies. *Nature Nanotechnology* **2019**, *14*, 80–88.

29. Salemmilani, R.; Piorek, B. D.; Mirsafavi, R. Y.; Fountain III, A. W.; Moskovits, M.; Meinhart, C. D. Dielectrophoretic Nanoparticle Aggregation for On-Demand Surface Enhanced Raman Spectroscopy Analysis. *Analytical Chemistry* **2018**, *90*, 7930–7936.

30. Dies, H.; Raveendran, J.; Escobedo, C.; Docoslis, A. *In Situ* Assembly of Active Surface-Enhanced Raman Scattering Substrates *via* Electric Field-Guided Growth of Dendritic Nanoparticle Structures. *Nanoscale* **2017**, *9*, 7847–7857.

31. Ge, T.; Yan, S.; Zhang, L.; He, H.; Wang, L.; Li, S.; Yuan, Y.; Chen, G.; Huang, Y. Nanowire Assisted Repeatable DEP–SERS Detection in Microfluidics. *Nanotechnology* **2019**, *30*, 475202.

32. Gao, Y.; Gan, Q.; Xin, Z.; Cheng, X.; Bartoli, F. J. Plasmonic Mach–Zehnder Interferometer for Ultrasensitive On-Chip Biosensing. *ACS Nano* **2011**, *5*, 9836–9844.

33. Feng, J.; Siu, V. S.; Roelke, A.; Mehta, V.; Rhieu, S. Y.; Palmore, G. T. R.; Pacifici, D. Nanoscale Plasmonic Interferometers for Multispectral, High-Throughput Biochemical Sensing. *Nano Letters* **2012**, *12*, 602–609.

34. Gao, Y.; Xin, Z.; Zeng, B.; Gan, Q.; Cheng, X.; Bartoli, F. J. Plasmonic Interferometric Sensor Arrays for High-Performance Label-Free Biomolecular Detection. *Lab on a Chip* **2013**, *13*, 4755–4764.

35. Fano, U. Effects of Configuration Interaction on Intensities and Phase Shifts. *Physical Review* **1961**, *124*, 1866.

36. Hao, F.; Sonnefraud, Y.; Dorpe, P. V.; Maier, S. A.; Halas, N. J.; Nordlander, P. Symmetry Breaking in Plasmonic Nanocavities: Subradiant LSPR Sensing and a Tunable Fano Resonance. *Nano Letters* **2008**, *8*, 3983–3988.

37. Neubrech, F.; Pucci, A.; Cornelius, T. W.; Karim, S.; García-Etxarri, A.; Aizpurua, J. Resonant Plasmonic and Vibrational Coupling in a Tailored Nanoantenna for Infrared Detection. *Physical Review Letters* **2008**, *101*, 157403.

38. Luk'yanchuk, B.; Zheludev, N. I.; Maier, S. A.; Halas, N. J.; Nordlander, P.; Giessen, H.; Chong, C. T. The Fano Resonance in Plasmonic Nanostructures and Metamaterials. *Nature Materials* **2010**, *9*, 707–715.

39. Giannini, V.; Francescato, Y.; Amrania, H.; Phillips, C. C.; Maier, S. A. Fano Resonances in Nanoscale Plasmonic Systems: A Parameter-Free Modeling Approach. *Nano Letters* **2011**, *11*, 2835–2840.

40. Sonnefraud, Y.; Verellen, N.; Sobhani, H.; Vandenbosch, G. A.; Moshchalkov, V. V.; Van Dorpe, P.; Nordlander, P.; Maier, S. A. Experimental Realization of Subradiant, Superradiant, and Fano Resonances in Ring/Disk Plasmonic Nanocavities. *ACS Nano* **2010**, *4*, 1664–1670.

41. Miroshnichenko, A. E.; Flach, S.; Kivshar, Y. S. Fano Resonances in Nanoscale Structures. *Reviews of Modern Physics* **2010**, *82*, 2257–2298.

42. Wu, C.; Khanikaev, A. B.; Adato, R.; Arju, N.; Yanik, A. A.; Altug, H.; Shvets, G. Fano-Resonant Asymmetric Metamaterials for Ultrasensitive Spectroscopy and Identification of Molecular Monolayers. *Nature Materials* **2012**, *11*, 69–75.

43. Brolo, A. G.; Gordon, R.; Leathem, B.; Kavanagh, K. L. Surface Plasmon Sensor Based on the Enhanced Light Transmission through Arrays of Nanoholes in Gold Films. *Langmuir* **2004**, *20*, 4813–4815.

44. Homola, J. Surface Plasmon Resonance Sensors for Detection of Chemical and Biological Species. *Chemical Reviews* **2008**, *108*, 462–493.

45. Yesilkoy, F.; Terborg, R. A.; Pello, J.; Belushkin, A. A.; Jahani, Y.; Pruneri, V.; Altug, H. Phase-Sensitive Plasmonic Biosensor Using a Portable and Large Field-Of-View Interferometric Microarray Imager. *Light: Science & Applications* **2018**, *7*, 17152–17152.

46. Belushkin, A.; Yesilkoy, F.; Altug, H. Nanoparticle-Enhanced Plasmonic Biosensor for Digital Biomarker Detection in a Microarray. *ACS nano* **2018**, *12*, 4453–4461.

47. Zhang, R.; Le, B.; Xu, W.; Guo, K.; Sun, X.; Su, H.; Huang, L.; Huang, J.; Shen, T.; Liao, T.; Liang, Y.; Zhang, J. X. J.; Dai, H.; Qian, K. Magnetic "Squashing" of Circulating Tumor Cells on Plasmonic Substrates for Ultrasensitive NIR Fluorescence Detection. *Small Methods* **2019**, *3*, 1800474.

48. Zhang, R.; Rejeeth, C.; Xu, W.; Zhu, C.; Liu, X.; Wan, J.; Jiang, M.; Qian, K. Label-free Electrochemical Sensor for CD44 by Ligand-Protein Interaction. *Analytical Chemistry* **2019**, *91*, 7078–7085.

49. Xu, W.; Wang, L.; Zhang, R.; Sun, X.; Huang, L.; Su, H.; Wei, X.; Chen, C.-C.; Lou, J.; Dai, H.; Qian, K. Diagnosis and Prognosis of Myocardial Infarction on a Plasmonic Chip. *Nature Communications* **2020**, *11*, 1654.

50. Haffner, C.; Chelladurai, D.; Fedoryshyn, Y.; Josten, A.; Baeuerle, B.; Heni, W.; Watanabe, T.; Cui, T.; Cheng, B.; Saha, S.; Elder, D. L.; Dalton, L. R.; Boltasseva, A.; Shalaev, V. M.; Kinsey, N.; Leuthold, J. Low-Loss Plasmon-Assisted Electro-Optic Modulator. *Nature* **2018**, *556*, 483–486.

51. Pelton, M. Modified Spontaneous Emission in Nanophotonic Structures. *Nature Photonics* **2015**, *9*, 427–435.

52. Kern, J.; Kullock, R.; Prangsma, J.; Emmerling, M.; Kamp, M.; Hecht, B. Electrically Driven Optical Antennas. *Nature Photonics* **2015**, *9*, 582–586.

53. Pein, B. C.; Chang, W.; Hwang, H. Y.; Scherer, J.; Coropceanu, I.; Zhao, X.; Zhang, X.; Bulovic, V.; Bawendi, M.; Nelson, K. A. Terahertz-Driven Luminescence and Colossal Stark Effect in CdSe–CdS Colloidal Quantum Dots. *Nano Letters* **2017**, *17*, 5375–5380.

54. Namgung, S.; Mohr, D. A.; Yoo, D.; Bharadwaj, P.; Koester, S. J.; Oh, S.-H. Ultrasmall Plasmonic Single Nanoparticle Light Source Driven by a Graphene Tunnel Junction. *ACS Nano* **2018**, *12*, 2780–2788.

55. Parzefall, M.; Novotny, L. Light at the End of the Tunnel. *ACS Photonics* **2018**, *5*, 4195–4202.

56. He, X.; Tang, J.; Hu, H.; Shi, J.; Guan, Z.; Zhang, S.; Xu, H. Electrically Driven Optical Antennas Based on Template Dielectrophoretic Trapping. *ACS Nano* **2019**, *13*, 14041–14047.

Graphical TOC Entry